\$ SUPER

Contents lists available at ScienceDirect

Materials Science & Engineering A

journal homepage: www.elsevier.com/locate/msea





Non-destructive evaluation of bulk material zones and interfaces in powder bed fusion additive manufactured Ti6Al4V

Teng Yang a,b, Mangesh V. Pantawane A, Yuqi Jin b, Narendra B. Dahotre a,**, Arup Neogi b,c,*

- a Department of Materials Science and Engineering, University of North Texas, Denton, TX, 76207, USA
- ^b Department of Physics, University of North Texas, Denton, TX, 76203, USA
- c Institute of Fundamental and Frontier Sciences, University of Electronic Science and Technology of China, Chengdu, China

ARTICLE INFO

Keywords: Laser powder bed fusion Ti64 Non-destructive evaluation Elasticity mapping Finite element analysis Interface acoustics

ABSTRACT

Inconsistency of equipment and inappropriate design in the laser powder-bed fusion additive manufacturing (LPBF-AM) process are not tightly related to the technology development and are more challenging to avoid. Those processing-related factors can introduce sudden changes in the products' local mechanical properties by internal flaws or microstructure variation. The different property zones and their interfaces will accumulate stress and decrease lifetime. In this work, we applied ultrasound elastography and density profile to evaluate an LPBF Ti6Al4V sample with three property zones induced by different laser speeds to represent equipment errors or inappropriate designs. The elastography clearly distinguished three zones and their corresponding dynamic properties. The ultrasound estimated density profile conforms with profilometer-determined values. The interfaces in the Ti64 sample between the zones were further discerned experimentally by ultrasound to determine the spatial and contrast distributions with a subwavelength resolution based on numerical simulations. The spatial profile and the contrast ratio on the upper boundary of the interface showed the correlation between the interface thickness and the cooling condition during the manufacturing process. These interfacial contrasts in mechanical properties within the bulk 3D printed material are challenging to detect by conventional non-destructive techniques.

1. Introduction

Laser powder bed fusion (LPBF) based additive manufacturing (AM) is one of the most widely used metal 3D printing methods since it manufactures optimized geometries, complex features, and intricate designs [1]. Ti6Al4V is a BCC + HCP lattice titanium alloy with low density. Due to its high strength, good fracture toughness, outstanding corrosion resistance, and exceptional biocompatibility [2], it has been widely used in aircraft structures [3], aerospace [4], automobile, marine [5], and biomedical engineering [6]. However, due to its poor thermal conductivity [7], the tendency to strain hardening [8], and aggressive chemical reactivity to oxygen [9], the fabrication of Ti6Al4V products is challenging. Traditional manufacturing processes inevitably result in significant waste material and higher manufacturing costs. Under such considerations, additive manufacturing is more suitable for fabricating Ti6Al4V products.

Nevertheless, due to its rapid thermokinetics nature, LPBF inevitably

encounters the issue of porosity control, residual stress, and hot cracking [10,11]. Although adjusting process parameters can alleviate these effects, traditional mechanical tests, such as tensile tests and hardness tests, are destructive during tests or sample preparation, which leads to some limitations since AM products are not easy to machine as a "dog-bone" shape tensile specimen due to high strength and the complex geometry. Advanced material characterization instruments like X-ray diffraction, scanning electron microscope (SEM), and electron backscattered diffraction (EBSD) have strict size limitations. All require extensive sample preparation steps involving machining and polishing that are time-consuming and could affect the inherent structure of the AM sample. Moreover, due to the microstructure heterogeneity, even a slight sample motion under high SEM magnification can lead to a distinct conclusion. Therefore, a deep understanding of the physics behind the process and a proper evaluation method for the final products help increase the quality of additively built items and offer reliable feedback on production processes for enhancing product quality [12].

E-mail addresses: narendra.dahotre@unt.edu (N.B. Dahotre), arupn@yahoo.com (A. Neogi).

^{*} Corresponding author. Department of Physics, University of North Texas, Denton, TX, 76203, USA.

^{**} Corresponding author.

Based on the above situations, non-destructive evaluation (NDE) is necessary to investigate the AM component's bulk elastic properties. Ultrasound NDE is a well-developed quality control and monitoring technique in aerospace [9,10], nuclear power industries [11], and materials research and development. It has been utilized to detect discontinuities and evaluate microstructure [13], grain size [14], porosity [15], and even residual stress [16]. The broad spectrum of process parameters in LPBF-AM enables the diagnostics of the bulk properties of the printed components under different settings [17,18]. It facilitates the understanding of the mechanisms that lead to the formation of internal flaws dictating the mechanical properties of AM material [19,20].

Although the relationship between process parameters and the physical properties of LPBF-AM products has been extensively studied [1,16,17], the effect of varying printing parameters in a single block and the information about the interfaces barely exists. Studying unexpected equipment flaws using the NDT/E methods for practical applications is important. Those instantaneous inconsistencies in the printing conditions can lead to a local zone with variations in the physical properties and interfaces relative to the surrounding materials. The laser scan speed was chosen as a variable factor to construct a layered cubic Ti6Al4V sample. It enables us to explore the relationship between manufacturing process parameters induced defects/microstructures difference in the LPBF sample and the effective density and dynamic elastic constant. A non-destructive ultrasound elastography technique, effective density, and dynamic bulk modulus elastography (EBME) [21] were used as the experimental NDE method. Much literature showed that acoustic wave propagation in metal/alloy mediums highly depends on the microstructure and micropores [22-24]. Even though the size of the features is much smaller than the acoustic wavelength, the overall effective changes in the bulk properties deviate from the sound wave behavior according to the effective medium approximation [25]. The EBME used acoustic wave propagation behavior to estimate bulk properties with local variation, including effective density and dynamic elastic constant, which overcame the conventional ultrasonic NDT limitation. In addition, we characterized the interface position and transition sharpness between the property zones using acoustic waves. At the interfaces, the microstructure changes in conventional microscopic imaging [26] is gradient and smooth. Furthermore, conventional

mechanical testing observed the interference from stress concentration [27]. Hence, both approaches cannot provide clear observation of the interface between the property zones. Ultrasound NDT can overcome the difficulty characterizing interfaces in laser powder bed fused samples in a mild observation scale.

2. Methods and materials

2.1. Laser powder-bed fusion additive manufactured Ti6Al4V block

The Ti6Al4V cubical block sample (26 mm \times 26 mm \times 26 mm) was printed in the AconityMIDI system shown in Fig. 1 (A). This system has a continuous wave Nd: YAG laser (Gaussian energy distribution) with a wavelength of 1070 nm and a laser diameter of around 80 μm . The Ti6Al4V powders were unimodal, extra-low interstitial Grade 23, with an average size of 15–45 μm . The composition of the powder is shown in Table 1.

The build chamber was maintained under an ultra-pure Argon gas atmosphere ($O_2 < 50$ ppm) throughout the LPBF-AM process. A single cubical block was printed using three sets of process parameters listed in Table 2. The power density of the laser is calculated according to equation = $\frac{p}{\nu \times h \times d}$, where P is laser power, ν scan speed, h hatch distance, and d layer thickness. Each set of process parameters printed 1/3rd of the cube and the configuration of three distinct property layers (top, middle, bottom) are shown in Fig. 1(B). The laser scanning direction was bidirectional (reversed after each track), and the scanning pattern was rotated by 90 ° between two successive layers, as Fig. 1 (C) on the left shows. The variation of scanning speed while maintaining the rest of the

Table 1Composition of Ti6Al4V Grade 23 powder.

| Titanium | Balance | Aluminum | 5.50–6.50 % | Vanadium | 3.50–4.50 % |
|----------|----------------|----------|----------------|-----------------|----------------|
| Iron | max 0.25 % | Oxygen | max 0.130 % | Carbon | max 0.080 % |
| Nitrogen | max 0.050 % | Hydrogen | max 0.013 % | Other, Total | max 0.40 % |

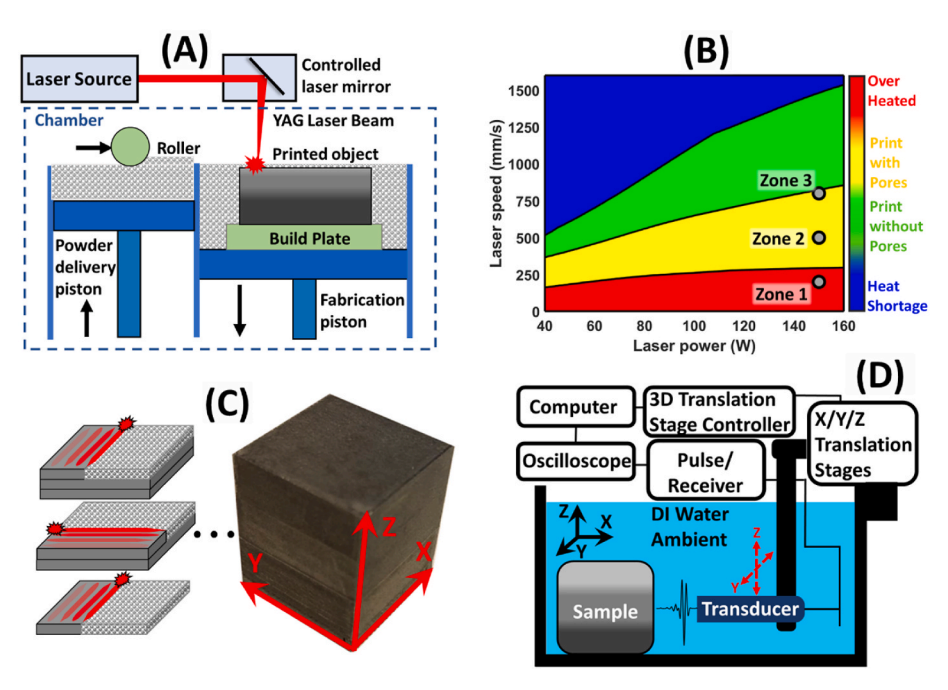


Fig. 1. Illustrations of the methods. (A). Laser melting powder-bed additive manufacturing. (B). Parameter selection is based on the summary from the literature [29]. (C). A bi-directional laser scan was performed in the printing process. The printed sample was shown in the photograph. Zones 1, 2, and 3 were vertically arranged along the building direction (Z). (D). Monostatic immersional raster scan setup for effective ultrasound density and dynamic Bulk modulus elastography.

Table 2
Processing parameter of Ti6Al4V block.

| | Power (W) | Speed (mm/s) | Hatch distance (µm) | Layer thickness (µm) | Power Density (W/ mm ³) |
|--------------------------|--------------|-----------------|---------------------------|----------------------------|---|
| Top Layer | 150 | 800 | 120 | 30 | 52.08 |
| Middle | 150 | 500 | 120 | 30 | 83.33 |
| Layer Bottom Layer | 150 | 200 | 120 | 30 | 208.33 |

parameters in three distinct regions is expected to affect the microstructure/phase formed in these regions significantly. The printed cubical block (Fig. 1C right) was detached from the circular build plate using electrode discharge machining for the post-process NDT and microstructural analysis. Each region of the printed block was analyzed using an optical microscope and scanning electron microscopy (SEM) by Thermofisher.

2.2. Effective density and dynamic Bulk modulus Elastography (EBME)

The EBME tests were performed in an acrylic water tank (500 mm imes400 mm \times 300 mm) filled with deionized water, as shown in Fig. 1 (D). The printed sample and the ultrasound transducer were immersed in the water. An Olympus Panametrics V316-N-SU planar emersion pencilstyle transducer with a 0.125-inch diameter at 20 MHz frequency was used to excite a broadband pulse from 13 to 27 MHz with a repetition rate of 200. The transducer was connected to the three-axis translation stages and controlled by the three-axis motion controller. A JSR Ultrasonic DPR 500 Pulse/Receiver is also adopted to control the pulse source and time trigger internally. A Tektronix MDO 3024b was applied to the collected testing data. The scanning process involved automated movement sequences of a transducer and data acquisition using a programmed MATLAB® script. The signal reflected from the sample during the raster scan was collected from 1281 locations, and at each location, the 512 signals were averaged to 1 recorded waveform in the oscilloscope. The scanning rate of each block was 512 signals in 20-s intervals. The resulting image area was 10 mm \times 4 mm at a 0.25 mm interval for both the building and filing axes. Further details about the EBME theory and calculation can be located in the literature [28].

2.3. Numerical simulation for the sensitivity of ultrasound to detect interface

In order to understand the sound wave propagation behavior at the interface of the distinct regions produced by the different sets of process parameters, finite element analysis (FEA) based on numerical simulations was performed. The acoustic module in COMSOL Multiphysics was used in this study. In the numerical model, the computational domain was divided into three regions: zone 1, interface, and zone 2. Zone 2 was assigned a 5 % higher bulk modulus (K2) than tn Zone 1 (K1). The bulk modulus at the interface region was arranged to vary linearly from K1 to K₂ along with the thickness of the interface. The model was solved using two parametric sweep studies. Firstly, by changing the interface thickness for fixed values of K1 and K2, 2. And secondly, by varying the K contrast (K₁ and K₂ difference) with a constant interface thickness. The height-dependent K profile of the gradient change interface was considered using the expression $K_{int}(x) = K_1 + (x - x_1)(K_2 - K_1)/(x_2 - K_1)$ x_1), where x indicates the position along the wave propagation direction, x_1 and x_2 were referred to as the position of the upper boundary of the K_1 zone and the lower boundary of the K_2 zone. The outer boundaries of the domain were assigned to impedance-matched conditions to eliminate the reflection sidewalls. The analytical equation of the acoustic source was a narrow pulse source emitted, in which the pulse envelope x(t) could be represented as a function by time t: x(t) =

 $\sin(2\pi f_0 t)e^{-f_0(t-\delta T_0)^2}$, where f_0 , T_0 and δ was the fundamental frequency (20 MHz), period (40 f_0^{-1}), and delay of the pulse signal, where δ was 1. The studied temporal interval was 0.125 T_0 . To represent the monostatic setup in experiments, a boundary probe detecting acoustic pressure on a linear scale was placed on the transducer to collect the reflection signals. In the results section, the acoustic intensity in the dB scale was referenced to the amplitude of the source pulse.

3. Result and discussion

Fig. 2A shows the EBME-generated contour plot of the dynamic bulk modulus of the LPBF-AM Ti6Al4V sample. These contour maps were measured from the YZ plane of the printed cube parallel to the build direction (Z-axis). The macroscopic elasticity variation of using different process parameters in a single block was established in the EBME contour plot (Fig. 2A). The dynamic bulk modulus in the bottom region was within a range of 101.5-103 GPa with an average modulus of 102 GPa. The corresponding bulk modulus for the middle region was higher in the range of 104-106 GPa, with an average value of 106 GPa. The dynamic bulk modulus further increased to 106-108 GPa in the top region, with an average value of 107.5 GPa. It can be noticed from Table 2 that laser energy density was increased linearly from the top to the bottom region of the printed cube. However, the dynamic bulk modulus did not change linearly, corresponding to the energy density. The softening effects reflected by dynamic bulk modulus values were around 1.5 GPa from the top to the middle layer and 4 GPa from the middle to the bottom, with a constantly increasing energy density. The non-linear variation of elastic modulus indicates the microstructure, phase transformation [32, 33], and porosity effect [34] due to changing process parameters. According to the effective media theory [25], the impedance mismatch from different porosity regions is more significant than grain boundaries and phase changes. Microstructural analysis was conducted at various levels to evaluate its rationale for contributing to elastic bulk modulus changes.

A profilometer image from the YZ-plane of the printed Ti6Al4V cube is presented in Fig. 2 (B). This high-resolution optical image clearly showed three distinct property regions by the porosity distribution, which was well-matched with the EBME effective bulk modulus contour plot in Fig. 2(A). The bottom region of the printed cube showed the highest fraction of porosity. The distribution was notably reduced in the middle region, and the top region rarely presents porosities. In Fig. 2(C), we calculated the horizontally averaged effective density values along the building direction (Z-axis) from the profilometer imaging and EBME effective density profile. The profilometer density profile presented along a vertical direction was obtained by horizontal pixel-counting in pre-prepared MATLAB codes. The 1D dark pixel fraction was then translated to 3D density values, assuming a sphere-shaped void. The comparison showed the agreement of zones' positions and density values. The EBME estimated effective density values had slightly more significant variations than the profilometer. Especially in Zone 3, the EBME effective density values are higher than the profilometer values relative to Zones 1 and 2. The slight overestimation can be attributed to the smaller grain size-induced acoustic energy loss in Zone 3 compared to Zones 1 and 2. Fig. 2(D) shows the magnified profilometer images of three layers, and the scale bar was set as 300 μ m. Table 3 summarizes the corresponding area porosity fraction and average size for each layer calculated by Image J software. With the increasing area porosity fraction from the top layer to the bottom layer, we expect a density decrease from the top layer to the bottom layer in confirmation with the EBME estimated effective density value. Moreover, it should be noted that as the laser density increased, the bottom regions fell into an over-melting zone that resulted in a much larger porosity size (Fig. 1(B)).

Fig. 3 presents the EBME contour plots obtained from the XY plane of the printed cube collected from various depths corresponding to the bottom region (Figure 3A), middle region (Fig. 3(B)), and top region

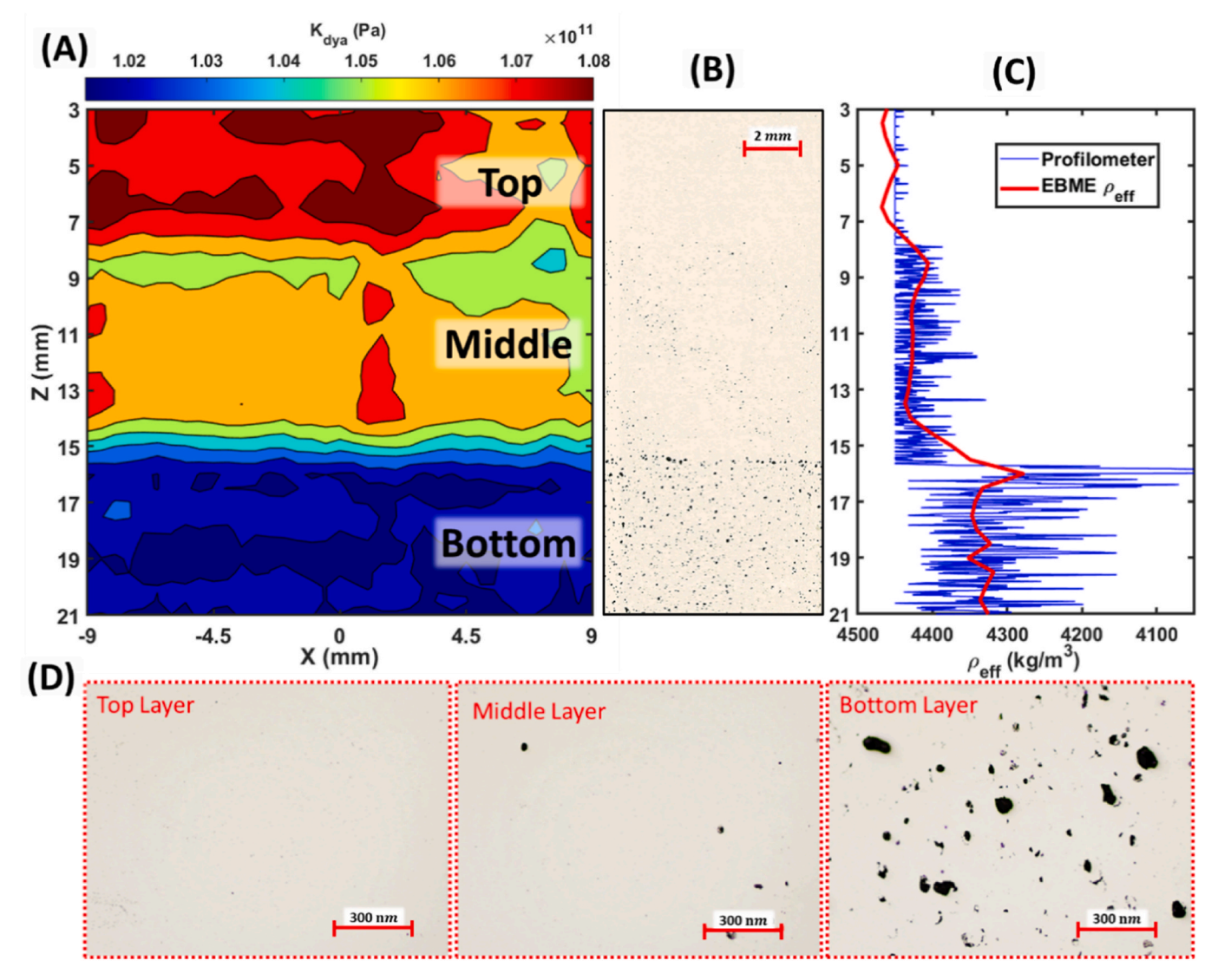


Fig. 2. Elastography and profilometer scan from the side view. (A). EBME scanned the dynamic bulk modulus map of the printed sample under as-built conditions. **(B).** Profilometer image of a central cut-out cross-section of the printed sample. **(C).** The estimated density comparison between the profilometer and EBME provided effective density along the building direction. **(D)** Magnetified images from the profilometer for each layer.

Table 3 Porosity fraction and average size for each layer.

| | Area fraction of Porosity | Average Porosity Size(nm) |
|---------------------|---------------------------|---------------------------|
| Top Layer | 0.28 % | 32.87 |
| Middle Layer | 1.84 % | 104.17 |
| Bottom Layer | 5.43 % | 422.32 |

(Fig. 3(C)). From the top view of ultrasound scans, the wave propagation is affected by more extended grain boundaries, which are contributed by the columnar grain structure along the built direction [30]. Hence, the dynamic bulk modulus from the top view presented slightly lower values than the side view (Fig. 2 (A)). The contrasts between the zones still agreed with the side view EBME (Figure 2(A)) and profilometer image (Fig. 2(B))). In the dynamic bulk modulus maps, we noticed the existence of 45° anisotropic property distribution, which was more significant in zones 2 and 3.

In the laser powder AM process, the transition between the two zones is microscopically gradual and smooth due to the higher melting depth with respect to the layer thickness [26]. It limits the evaluation of the interface using conventional observation techniques. Especially in a

single material-based interface, the lack of transient composition introduced more challenges in the characterization due to the low contrast of the physical properties. Fortunately, conventional time-of-flight ultrasonic discontinuity detection methods offer an alternative plan to locate the material interface and evaluate the transient sharpness. An additional reflection from the interface is necessary to obtain information about a material's interface adequately. However, the characterization capability of the time-of-flight methods regarding interface thickness and property change degree is unclear. Therefore, we conducted numerical simulations on the ultrasonic detection of the gradient changes of the property interfaces to understand and verify the sensitivity of the detection methodology.

In addition to the porosity, microstructural/phase variation also contributes to the ultrasound energy variation within the printed sample. Such microstructural or phase variation in each region was identified using scanning electron microscopy. Fig. 3D1-2, 3E1-2, and 3F1-2 present the SEM image

corresponding to the top, middle, and bottom regions of the LPBF-AM Ti6Al4V. The top region with fabrication of low energy density mainly showed the presence of martensite laths (Fig. 3F1 and 3F2). The formation of martensite lath can be attributed to the rapid cooling rate

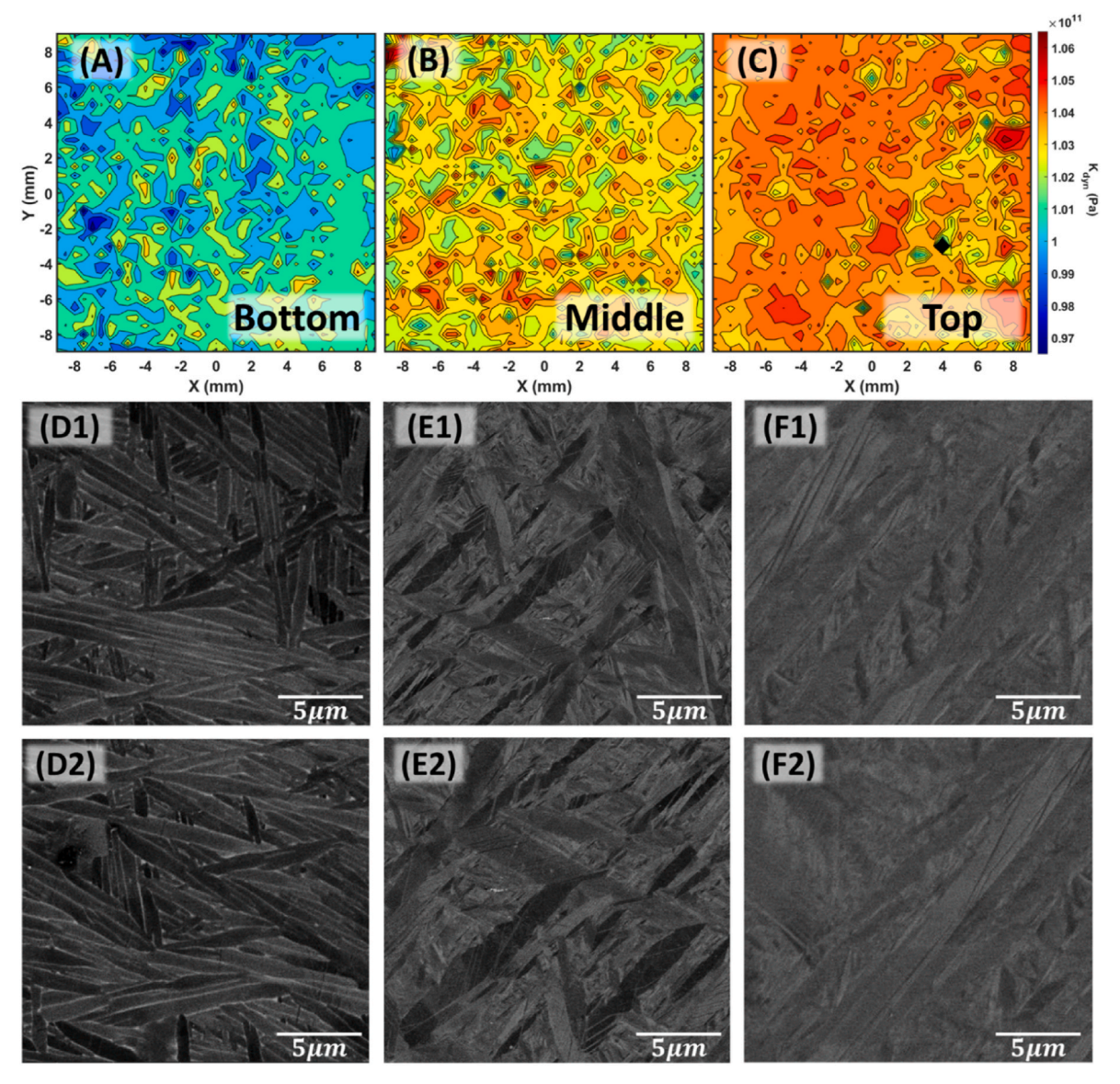


Fig. 3. Elastography from the top view. (A–C). EBME scanned dynamic bulk modulus map of the printed sample (Zones 1–3) under as-built conditions. (D1 and D2). SEM images of the printed sample at Zone 1 (bottom region) under as-built conditions. (E1 and E2). SEM images of the printed sample at Zone 2 (middle region) under as-built conditions. (F1 and F2). SEM images of the printed sample at Zone 3 (top region) under as-built conditions.

induced during the laser powder-bed fusion process. Based on the computational thermokinetic model developed in the earlier reports of the authors, these cooling rates were predicted in the range of 10^{5-7} K/s. With the increase in the energy density by reducing the laser scanning speed, the middle region showed partial decomposition of the martensite lath, leading to the nucleation of β precipitates at a few locations along the interface of the martensite (Fig. 3E1 and 3E2). With the highest laser energy density employed in the bottom region of the cube, the martensite appeared to decompose completely into α and β phases. The microstructural evolution due to increased energy input leading to the formation of the β phase will likely reduce the bulk modulus. The β phase is a base-centered cubic (BCC) lattice structure with a relatively open lattice structure than the hexagonal closed packed (HCP) lattice. It increases the average interatomic spacing in the BCC lattice phase, reducing the material's elastic modulus.

3.1. The detection capability of the time-of-flight technique on interfaces

Due to the diffraction limit, ultrasonic diagnostics techniques cannot detect the presence of voids with a dimension smaller than the operating

wavelength of acoustic waves. However, according to the effective media theory, the acoustic wave has different propagation behavior in the different physical property regions. Such behaviors are frequency-dependent on the effective physical properties in the medium, which was the principle of the experimental ultrasound elastography shown in Figs. 2 and 3. Hence, a slight variation in the elastic constant or density can be used as a generalized function to represent the distinguishable property zones, including the influence of the microstructure and microvoids. Modifying the acoustic wave interaction at the interface of two property zones provides significant information about the instability-induced local property change in the practical AM products.

As Fig. 4 (A_1 - A_4) illustrates, we designed two material regions with a 5 % difference in bulk modulus. The bulk modulus of the transition zone at the interface was designed to increase linearly from K_1 to K_2 . Fig. 4 A_1 - A_4 depict the selected bulk modulus distribution maps from a parametric study on the interface thickness D from 0.01 operating wavelength (λ) to 2 λ . In Fig. 4 B_1 - B_4 , the identical acoustic pulse sources were injected into the upper material layers by the transducers that propagate into the interfaces. In Fig. 4 C_1 - C_4 , we can observe that the interface-induced reflection was visible when the interface thickness was smaller than

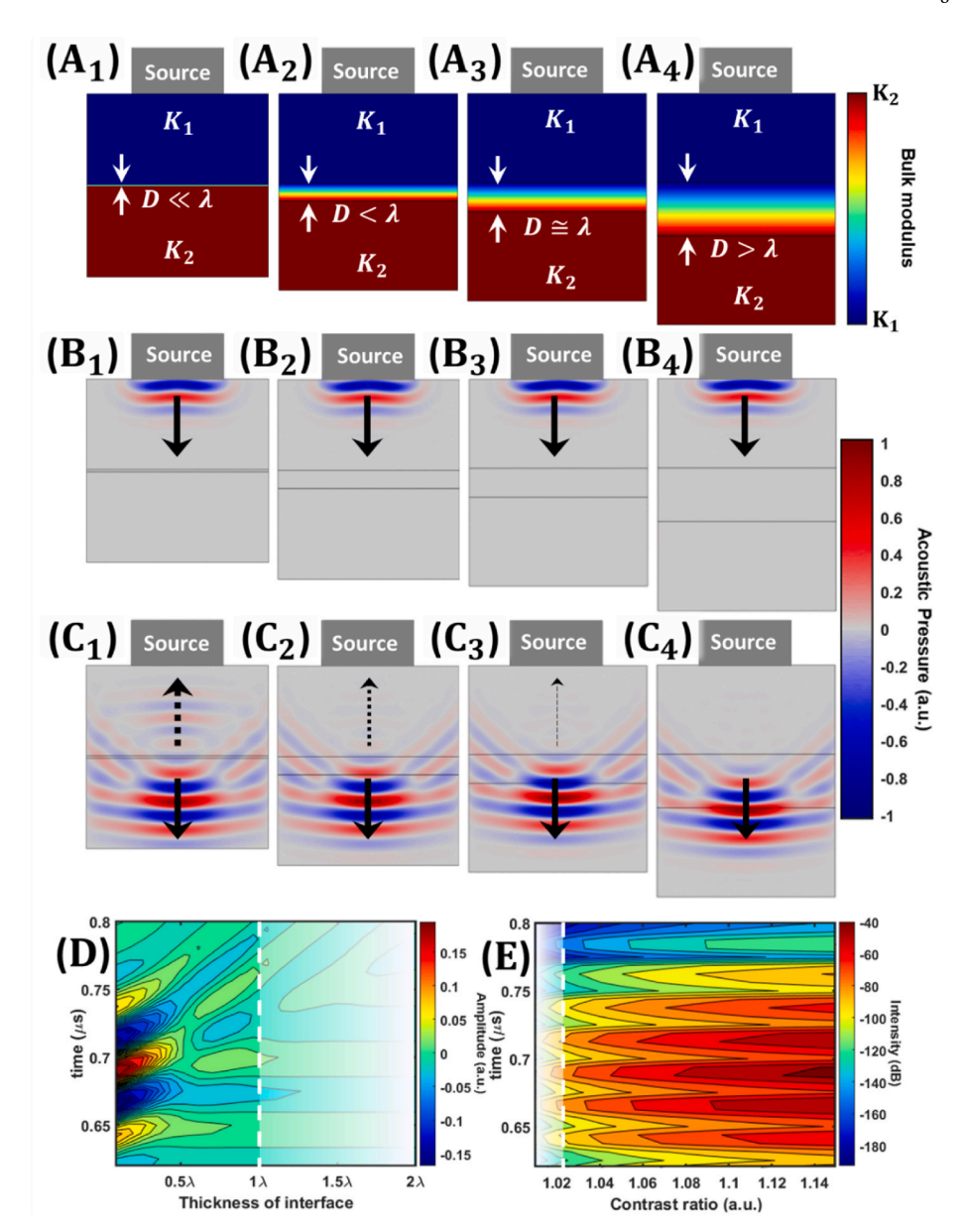


Fig. 4. Numerical simulation of sound wave behavior on the interface with gradient varying property. (A). Assigned bulk modulus distribution of the model with interface thickness sweeping. (B). Identical ultrasound pulses were emitted from the transducer propagating toward the interfaces at time point t_1 from the view of acoustic pressure profiles. (C). Acoustic pressure maps demonstrated transmitted and reflected pulses at the interfaces at time point t_2 . (D). Interface thickness-dependent reflection pulse amplitude, where λ is the operating wavelength. (E). Bulk modulus contrast ratio (K_2/K_1) dependent acoustic intensity of the interface-produced reflection pulse.

the operating wavelength (C_1 and C_2). The echo became negligible when D was comparable with and larger than λ (C_3 and C_4), where the Cummer–Schurig liked acoustic cloaking [31] occurred.

In Fig. 4 (D), we summarized the collected reflection signal produced from the interface in the simulation. When the interface thickness was within 0.4 λ , the reflection amplitude was inversely proportional to the interface thickness. Between 0.4 and 1 λ , a significant dispersion can be observed on the pulse envelope. The dispersion-induced out-of-phase effect further decreased the reflection signal amplitude. Beyond the 1 λ (white shadow area), when cloaking occurs at the interface, the reflection signal becomes immeasurable. In Fig. 4(E), we conducted another parametric study on the bulk modulus contrast ratio K_2/K_1 with fixed interface thickness $D^{''}\lambda$. In this contour, the collected reflection signal is represented in terms of intensity to estimate the material contrast ratio-dependent detection feasibility. As the results showed, in a thin enough interface, the acoustic intensity of the echo approached -90 dB when K_2

is 2 % higher than K_1 . This signal intensity was about the minimum detection feasibility in the experimental case when the noise level is usually at -100 to -110 dB without any advanced signal amplifier or signal processing techniques.

Numerical simulation reveals that the amplitude of the gradient interface-induced acoustic reflection was proportional to the material contrast ratio K_2/K_1 and inversely proportional to the interface thickness D. Here, we defined a dimensionless factor interface sharpness factor $\chi=p_{if}/p_0$, where p_{if} is the signal amplitude of the interface reflection, and p_0 was the source pulse amplitude. The sharpness factor $\chi \propto \frac{K_2}{K_1} D^{-1}$ and was applied to describe the transition sharpness on the interfaces in our LPBF Ti64 block.

In Fig. 5, we plotted the experimentally obtained interface information from the Ti64 sample using a long enough operating wavelength ultrasound wave. The ultrasound wave was excited from the upper surface (zone 3) into the block sample. The vertical axis indicates the

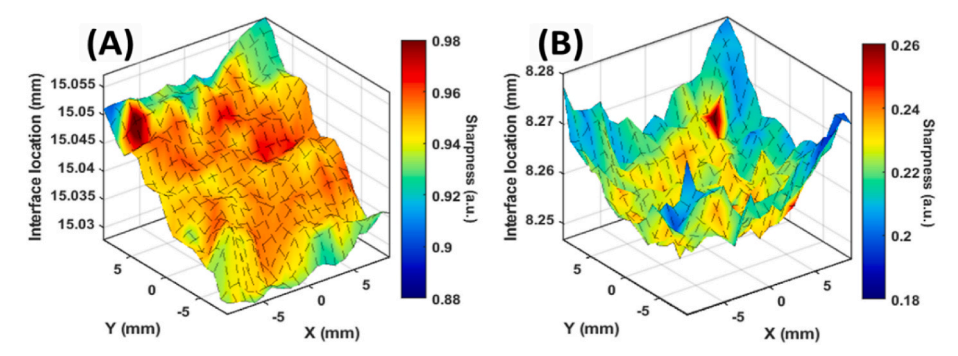


Fig. 5. Experimentally estimated upper interface boundary location and contrast ratio using ultrasound on the printed sample. (A). Interface behavior between zones 1 and 2. (B). Interface behavior between zones 2 and 3.

position of the interface provided echo along the building axis. The rainbow color scale presents the normalized interface sharpness distribution we proposed in the previous section. We noted that the 3D contours showed the interface location profiles of the upper boundary of the interfaces. The bottom boundaries of the transient regions were considered to be horizontally flat interfaces when the processing parameter changed along the built direction. During the diagnostics, the acoustic wave propagates from the top surface of the sample to its bottom surface, opposite the building direction of the block. The additional reflection pulse from the interface was obtained from the near boundaries respected to the acoustic source.

Fig. 5(A) shows the upper interface profile between Zone 1 and 2. The interface shows a spatial inclination along the diagonal from location (-9, -9) to (9, 9) around 25 µm, which was possibly due to the wrapped edge and the wrapped corner (about 0.5 mm) on the bottom of the block (zone 3). The sharpness profile on this interface showed a higher contrast around the central region than the corners. It is possibly caused by a rapid transition from central zone 1 to central zone 2 in terms of microstructure size and void fraction under better cooling conditions. The inclined behavior can be attributed to the lower cooling rate at the wrapped corner region, forming the microstructure and micropores-induced transition that takes longer to approach thermal equilibrium. The interface profile between zone 2 and 3 was plotted in Fig. 5 (B). The spatial profile and the sharpness map of this interface exhibit a symmetry along the central axis. The central region of the interface was transited at a shorter distance than the corners. This behavior further confirms the phenomenon of cooling rate-dependent interface thickness.

4. Conclusion

In this study, we intentionally introduced three zones in an LPF AM Ti64 cube by varying the laser scan speed. The fabricated sample was inspected by ultrasound elastographic technique, providing the dynamic bulk modulus distribution and effective density profile. The ultrasoundtested effective density profile showed agreement with the laser-sourced profilometer results, which has never been demonstrated in the existing literature. Furthermore, the interface between the local property zones (additional echo occurrence) was the key target for ultrasound NDT/E detecting flaws. Hence, the two interfaces between the three physically different characteristic layers in our cube were also studied in this work. The experimental method was first studied by interface acoustics simulation to estimate the technique's feasibility and limitations. After the verification, the methods were experimentally applied in the Ti64 cube with the property layers. The results showed that, along the building direction, the upper boundaries of the interfaces were not as horizontally flat as we expected. The spatial profile and the contrast ratio on the upper boundary of the interface showed the correlation between the interface thickness and the cooling condition during the process.

Ethics approval

This manuscript is not under consideration for publication elsewhere. All the results presented in this work are unpublished. All ethical guidelines have been followed.

Consent to participate

Not applicable.

Consent for publication

All authors have reviewed the manuscript and provided their consent for publication.

CRediT authorship contribution statement

Teng Yang: Formal analysis, Investigation, Methodology, Validation, Visualization, Writing – review & editing. Mangesh V. Pantawane: Data curation, Methodology. Yuqi Jin: Conceptualization, Data curation, Formal analysis, Investigation, Writing – original draft. Narendra B. Dahotre: Project administration, Supervision, Validation, Visualization, Writing – review & editing. Arup Neogi: Methodology, Project administration, Supervision, Visualization, Writing – review & editing.

Declaration of competing interest

The authors declare that they have no known competing financial interests or personal relationships that could have appeared to influence the work reported in this paper.

Data availability

Data will be made available on request.

Acknowledgment

This work is supported by EFRI Grant No. 1741677 from the National Science Foundation.

References

- C.L. Druzgalski, A. Ashby, G. Guss, W.E. King, T.T. Roehling, M.J. Matthews, Process optimization of complex geometries using feed-forward control for laser powder bed fusion additive manufacturing. Addit. Manuf. 34 (2020), 101169.
- [2] S. Liu, Y.C. Shin, Additive manufacturing of Ti6Al4V alloy: a review, Mater. Des. 164 (2019), 107552.
- [3] P. Singh, H. Pungotra, N.S. Kalsi, On the characteristics of titanium alloys for the aircraft applications, Mater. Today: Proc. 4 (8) (2017) 8971–8982.

- [4] I. Inagaki, T. Takechi, Y. Shirai, N. Ariyasu, Application and features of titanium for the aerospace industry, Nippon Steel Sumitomo Metal Tech. Rep. 106 (106) (2014) 22–27
- [5] I. Gurrappa, Characterization of titanium alloy Ti-6Al-4V for chemical, marine and industrial applications, Mater. Char. 51 (2–3) (2003) 131–139.
- [6] C. Emmelmann, P. Scheinemann, M. Munsch, V. Seyda, Laser additive manufacturing of modified implant surfaces with osseointegrative characteristics, Phys. Procedia 12 (2011) 375–384.
- [7] L. Parry, I.A. Ashcroft, R.D. Wildman, Understanding the effect of laser scan strategy on residual stress in selective laser melting through thermo-mechanical simulation, Addit. Manuf. 12 (2016) 1–15.
- [8] R.K. Gupta, V.A. Kumar, C. Mathew, G.S. Rao, Strain hardening of titanium alloy Ti6Al4V sheets with prior heat treatment and cold working, Mater. Sci. Eng., A 662 (2016) 537–550.
- [9] M.N. Mungole, S. N, G.N. Mathur, Oxidation behavior of Ti6Al4V titanium alloy in oxygen, Mater. Sci. Technol. 18 (1) (2002) 111–114.
- [10] H.Z. Yu, R.S. Mishra, Additive friction stir deposition: a deformation processing route to metal additive manufacturing, Mater. Res. Lett. 9 (2) (2021) 71–83.
- [11] X. Zhou, N. Dai, M. Chu, L. Wang, D. Li, L. Zhou, X. Cheng, X-ray CT analysis of the influence of the process on defect in Ti-6Al-4V parts produced with Selective Laser Melting technology, Int. J. Adv. Des. Manuf. Technol. 106 (1) (2020) 3–14.
- [12] T. Yang, S. Mazumder, Y. Jin, B. Squires, M. Sofield, M.V. Pantawane, N. B. Dahotre, A. Neogi, A review of diagnostics methodologies for metal additive manufacturing processes and products, Materials 14 (17) (2021) 4929.
- [13] K.M.S. Levy, J.-Y. Kim, L.J. Jacobs, Investigation of the relationship between classical and nonclassical ultrasound nonlinearity parameters and microstructural mechanisms in metals, J. Acoust. Soc. Am. 148 (4) (2020) 2429–2437.
- [14] I. Markja, K. Dhoska, D. Elezi, R. Moezzi, M. Petru, Effect of the grain sizes on the ultrasonic propagation and attenuation on different types of steels microstructure during non-destructive testing, Ann. Chimie Sci. Matériaux 45 (4) (2021) 329–334.
- [15] G. Diot, A. Koudri-David, H. Walaszek, S. Guégan, J. Flifla, Non-destructive testing of porosity in laser welded aluminum alloy plates: laser ultrasound and frequencybandwidth analysis, J. Nondestr. Eval. 32 (4) (2013) 354–361.
- [16] R. Acevedo, P. Sedlak, R. Kolman, M. Fredel, Residual stress analysis of additive manufacturing of metallic parts using ultrasonic waves: state of the art review, J. Mater. Res. Technol. 9 (4) (2020) 9457–9477.
- [17] J. Beuth, N. Klingbeil, The role of process variables in a laser-based direct metal solid freeform fabrication. Jom 53 (9) (2001) 36–39.

- [18] C.U. Brown, Gregor Jacob, A. Possolo, C. Beauchamp, M. Peltz, M. Stoudt, A. Donmez, The Effects of Laser Powder Bed Fusion Process Parameters on Material Hardness and Density for Nickel Alloy 625, US Department of Commerce, National Institute of Standards and Technology, 2018.
- [19] S. Tammas-Williams, P.J. Withers, I. Todd, P.B. Prangnell, The influence of porosity on fatigue crack initiation in additively manufactured titanium components, Sci. Rep. 7 (1) (2017) 1–13.
- [20] M. Seifi, A. Salem, D. Satko, J. Shaffer, J.J. Lewandowski, Defect distribution and microstructure heterogeneity effects on fracture resistance and fatigue behavior of EBM Ti-6Al-4V, Int. J. Fatig. 94 (2017) 263–287.
- [21] Y. Jin, E. Walker, A. Krokhin, H. Heo, T.-Y. Choi, A. Neogi, Enhanced instantaneous elastography in tissues and hard materials using bulk modulus and density determined without externally applied material deformation, IEEE Trans. Ultrason. Ferroelectrics Freq. Control 67 (3) (2019) 624–634.
- [22] T. Wan, T. Naoe, T. Wakui, M. Futakawa, H. Obayashi, T. Sasa, Effects of grain size on ultrasonic attenuation in type 316L stainless steel, Materials 10 (7) (2017) 753.
- [23] Y. Liu, Q. Tian, X. Guan, Grain Size Estimation Using Phased Array Ultrasound Attenuation, NDT & E International, 2021, 102479.
- [24] M. Nori, S. Brandani, A simplified model for acoustic measurement of diffusion in microporous solids, Adsorption 1 (433) (2005) 11.
- [25] A.A. Krokhin, J. Arriaga, L.N. Gumen, Speed of sound in periodic elastic composites, Phys. Rev. Lett. 91 (26) (2003), 264302.
- [26] R. Anderson, J. Terrell, J. Schneider, S. Thompson, P. Gradl, Characteristics of bimetallic interfaces formed during direct energy deposition additive manufacturing processing, Metall. Mater. Trans. B 50 (4) (2019) 1921–1930.
- [27] Y. Jin, T. Wang, A. Krokhin, T.-Y. Choi, R.S. Mishra, A. Neogi, Ultrasonic elastography for nondestructive evaluation of dissimilar material joints, J. Mater. Process, Technol. 299 (2021), 117301.
- [28] Y. Jin, E. Walker, H. Heo, A. Krokhin, T.-Y. Choi, A. Neogi, Nondestructive ultrasonic evaluation of fused deposition modeling based additively manufactured 3D-printed structures, Smart Mater. Struct. 29 (4) (2020), 045020.
- [29] H. Gong, K. Rafi, H. Gu, T. Starr, B. Stucker, Analysis of defect generation in Ti-6Al-4V parts made using powder bed fusion additive manufacturing processes, Addit. Manuf. 1 (2014) 87–98.
- [30] M.V. Pantawane, T. Yang, Y. Jin, S.S. Joshi, S. Dasari, A. Sharma, A.e. a. Krokhin, Crystallographic texture dependent bulk anisotropic elastic response of additively manufactured Ti6Al4V, Sci. Rep. 11 (1) (2021) 1–10.
- [31] L.-W. Cai, J. Sánchez-Dehesa, Analysis of cummer–schurig acoustic cloaking, New J. Phys. 9 (12) (2007) 450.